PORE NETWORK MODELLING ON CARBONATE: A COMPARATIVE STUDY OF DIFFERENT MICRO-CT NETWORK EXTRACTION METHODS

Hu Dong, Ståle Fjeldstad, Luc Alberts, Sven Roth, Stig Bakke and Pål-Eric Øren
Numerical Rocks AS, Trondheim, Norway

This paper was prepared for presentation at the International Symposium of the Society of Core Analysts held in Abu Dhabi, UAE 29 October-2 November, 2008

ABSTRACT

In this work we compare four different methods to extract topological skeletons from three dimensional (3D) images of porous media. The applied methods are: (i) medial axis, (ii) maximal ball, (iii) velocity based, and (iv) grain recognition based algorithms. The methods are applied to 3D rock microstructure images of both sandstones and carbonates. The images were obtained from process based reconstructions and X-ray micro-tomography. From the computed skeletons, the complete pore network representations are generated using the same geometrical partitioning and analysis algorithms. The networks are compared in terms of key morphological parameters (connectivity, pore and throat size distribution). The petrophysical properties, i.e. permeability and formation factor, predicted by the networks are compared with the results that are calculated directly on the voxel based images. Predicted primary drainage and waterflood relative permeabilities for water wet conditions are computed and compared for one sandstone and two carbonate samples. We show the agreement and discrepancies of the predictions from these different methods. The results are compared and related to the structures of the extracted networks.

INTRODUCTION

The microstructure of a porous rock largely controls its flow, electrical and acoustic properties. Although the topology and geometry of the pore structure is complex, transport properties can be predicted through the use of simplified network models (Øren et.al., 1998; Patzek, 2001; Blunt et.al., 2002). The premise of a network model is that the complex pore structure can be represented by an equivalent network of interconnected pores in which larger pores (pore bodies) are connected via smaller pores (pore throats). Although the level of details necessary to predict a given property can differ, the actual pore structure must always be mapped onto a network structure. Direct mapping of a pore structure requires some method for acquiring three-dimensional descriptions of the actual rock of interest. In recent years, several methods have been made available for obtaining such descriptions. Direct measurements of a rock microstructure are now available via X-ray micro-tomography (Spanne et.al., 1994; Arns et.al., 2004). A complementary tool to micro-tomography is process based models which simulates the actual rock forming processes (Bakke and Øren, 1997, Øren and Bakke, 2002).

The most critical and difficult part of constructing an equivalent network is to identify the topological skeleton, i.e. specifying the pore bodies and throats. A number of algorithms have been proposed for skeleton extraction. These algorithms fall into two main classes. The first works directly on the pore space and are based on either medial axis transform (e.g. Lindquist et.al., 1996) or maximal balls (e.g. Silin and Patzek, 2006). The second exploits the complementarity of the pore and grain spaces and are based on Delaunay or Voronoi tessellation (e.g. Bryant et.al., 1993; Øren and Bakke, 2002). Application of the latter algorithms requires knowledge of the grain locations. If these are not known, the grain space must first be partitioned before extracting the skeleton.

In this work we apply and compare different methods for extracting topological skeletons from 3D rock microstructure images of sandstones and carbonates. The methods that we apply are based on: (i) medial axis transform, (ii) maximal balls, and (iii) grain recognition followed by Voronoi tessellation. We also present a new method (iv) that is based on 3D thinning of the velocity field in the pore space. The velocity field is calculated from a solution of the Stokes equations directly on the rock microstructure image. The pore networks generated by these four methods are compared in terms of morphological parameters, single phase properties, and multiphase flow parameters.

SKELETONIZATION METHODS

Below we briefly describe the four methods we applied to extract topological skeletons from 3D rock microstructure images. Detailed descriptions of the different algorithms can be found in the references.

Medial axis based method

The medial axis based method (denoted MA) transforms the pore space into a medial axis that is the topological skeleton of the pore space running roughly along its geometric middle (Lindquist et.al., 1996; Sheppard et.al., 2005). The medial axis can be obtained by a morphological thinning algorithm (Baldwin et.al., 1996; Liang et.al., 2000) or a pore space burning algorithm (Lindquist et.al., 1996), by which the pore space is eroded from the grain surfaces until the burning from different directions ends up in one voxel. In this study, the MA method is implemented by using the skeletonization function in a commercial software Avizo (earlier called Amira), which is based on a hybrid algorithm that combines thinning and distance map based techniques called *Distance Ordered Homotopic Thinning* (Youssef et.al., 2007). To obtain a consistent comparison of the topological features of the four different methods, the output skeletons are directly used without pruning the branches induced by surface irregularities and image noise. The MA method in our tests seems to introduce spurious nodes, which could be eliminated by removing the corresponding false branches in the skeleton.

Maximal ball method

The maximal ball (denoted MB) based algorithm (Silin and Patzek, 2006; Al-Kharusi and Blunt, 2007; Dong, 2007) finds the largest inscribed spheres at each voxel in the pore space and removes those included in other spheres. Those remaining are called maximal balls and

describe the pore space without redundancy. The maximal balls are constructed and hierarchized by a clustering process (Dong, 2007) to define pores and throats by affiliating the maximal balls into family trees according to their size and rank (the sequence being connected to earlier defined branches on the family trees). The ancestor of each family tree defines the pore and the common child defines the throats. The skeleton is generated during the clustering as mainstream branches on the family trees.

Flow velocity based method
The flow velocity based method (denoted VB) generates a pore skeleton by tracking the fastest path for laminar flow through the pore space of the rock. Using 3D computational fluid dynamics the flow velocity is calculated for all voxels in the pore-space of the rock (Øren et.al., 2006). The pore skeleton is then extracted by doing greyscale 3D thinning on the pore space, where each pore voxel is represented by a scalar proportional to the maximal flow velocity at the voxel. The maximal flow velocity equals the maximum of the flow velocities in all 18 directions in an 18-connected lattice. The intersections on the skeleton define the link-node or node-link interfaces, where a single flow path splits up, or multiple flow paths are joined into a single flow path.

Grain recognition based method
Contrary to the other three methods, the grain recognition based method (denoted GR) starts by partitioning the solid phase to identify the granular structure (Thompson et. al., 2005). Once the solid voxels have been grouped into individual grains by Euclidian distance transformation, the grain centers are identified using the maximum inscribed sphere and solid phase partitioning. When the grains have been identified, the pore space can then be divided into polyhedra using Voronoi tessellation (Øren and Bakke, 2003). The edges of the Voronoi polyhedra define the pore skeleton.

SAMPLES

The samples analysed include 3D rock microstructure images of both sandstones and carbonates. The images were obained from process based reconstructions (denoted PB) and X-ray micro-tomography (denoted MCT). The PB images include a regular sphere packing (P1) and two Fontainebleau sandstones (F11 and F22). The MCT images are two carbonates (C1 and C2) and one reservoir sandstone (S1). Cross-sections of the PB and MCT samples are shown in Figures 1 and 2, respectively.

P1: The regular sphere packing P1 contains 490 spherical grains with uniform radii of 32 µm and 1.6 µm overlapping of each grain. The unit cell contains eight grains in a rhombohedral-hexagonal arrangement. The pack has an image resolution of 1µm and a porosity of 12.1%, representing a volume of 375^3 μm^3.

F11 and F22: The two reconstructed (Øren and Bakke, 2002) Fontainebleau samples, F11 and F22, have porosity of 11% and 22%, respectively. The high porosity image has a resolution of 5 µm. The resolution of the low porosity images is 2.5 µm. The extracted sample size is the same for both models (3.375 mm^3).

Figure 1. From left to right: cross-sectional images of sample P1, F11 and F22 generated using the PB method. The side lengths are 0.375 mm, 1.5 mm and 1.5 mm respectively. In the images, black is the pore space; white is the quartz grain.

Figure 2. From left to right; cross-sectional images of the MCT samples C1, C2 and S1. The side lengths are 0.84 mm, 1.55 mm and 2.68 mm, respectively. In the images, black is the pore space; grey is clay; and white is the solid matrix.

C1: C1 is a vuggy replacement dolostone without fabrics preservation, consisting of sub- and euhedral dolomite crystals. Solution-enlarged irregular intercrystal porosity indicates post dolomite calcite dissolution. Large vugs are probably biomolds. Abundant patchy, poikilotopic anhydrite cement is present. The image resolution is 1.4 μm consisting of 600^3 voxels across a volume of 0.6 mm^3. The segmented porosity is 33%. The measured permeability of the larger core sample is 460 mD.

C2: This outcrop sample of Mt Gambier limestone (Oligocene – Miocene) is a high porosity, cool-water bryozoan-rich grainstone with accessory benthonic foraminifera and echinoids from South Australia. The image was obtained from the Australian National University. The image contains 512^3 voxels with a resolution of 3.024 μm and segmented porosity of 43.6%.

S1: The sandstone sample is a poorly sorted channel sandstone with angular to sub-angular grains of low to medium sphericity. The grain size ranges from very fine sand to coarse sand. The rock consists of approximately 61% quartz, 10% poikilotopic carbonate cement and 8-9% clay. The intergranular porosity is around 20%. The image contains 512^3 voxels with a resolution of 5.24 μm representing a rock volume of 19.3 mm^3.

STRUCTURAL COMPARISONS

Having determined the skeleton, i.e. identified all the pore bodies and throats, we next applied geometric partitioning and analysis to construct the complete pore network representation. Details about the geometrical analysis and the morphological parameters used in the network representation are given elsewhere (Øren and Bakke, 2003). Below we compare key morphological parameters of the extracted networks.

Numbers of pores and throats and their connectivity

Table 1 summarises the numbers of pores and throats identified in the various networks. For all the samples, there are large variations in the number of pores identified by the different algorithms. This illustrates the sensitivity of the different methods to image noise and geometrical complexity of the pore space. The VB method tends to produce the largest number of pores and throats, which indicates that the method is responsive to geometrical details. The VB method is of course also sensitive to the accuracy of the computed velocity profile. This, in turn, depends strongly on the image quality.

The MA network for sample S1 is clearly different from the others. It contains roughly 5 times as many pores as the networks extracted by the other methods. This suggests that the applied MA method is not able to produce an accurate representation of the pore structure. Sample S1 has a high level of image noise, mainly due to the presence of clay (8-9%) and insufficient image resolution to accurately capture smaller pores.

Table 1. Numbers of the pores and throats in the networks extracted using MA, GR, MB and VB methods. The numbers of throats are in brackets.

Samples	P1	F11	F22	C1	C2	S1
MA	1028 (2367)	2501 (2991)	1560 (2415)	67623 (100470)	3924 (5765)	75055 (41886)
GR	1455 (2869)	2005 (2433)	1676 (2824)	50863 (99865)	4763 (6623)	9810 (9277)
MB	1110 (2462)	1496 (2109)	1516 (2861)	53487 (107727)	3994 (6160)	14709 (20559)
VB	1952 (3353)	4027 (6102)	2492 (4286)	62745 (128896)	4643 (7603)	16749 (28656)

The network topology or connectivity is expressed by the coordination number, i.e. the number of throats connected to a pore body. Table 2 summarises the average and maximum coordination numbers of the networks. The corresponding distributions can be found in Figure 3. For the regular sphere packing P1, all the methods successfully identify the interior pores, i.e. pores with coordination number 4 and 8. However, differences are found on the sides of the image due to different schemes for handling boundary effects. The GR and VB methods tend to define more 1- and 2-connected pores on the P1 image boundaries, resulting in lower average coordination number.

Table 2. Average and maximum (in brackets) coordination numbers of the networks using MA, GR, MB and VB methods.

Samples	P1	F11	F22	C1	C2	S1
MA	5.3 (8)	2.5 (13)	3.4 (13)	3.0 (132)	3.2 (92)	1.1 (64)
GR	4.5 (8)	2.6 (10)	3.8 (14)	4.0 (149)	3.0 (119)	2.0 (41)
MB	5.1 (8)	3.1 (10)	4.3 (12)	4.1 (122)	3.3 (83)	2.9 (31)
VB	4.0 (9)	3.2 (22)	3.8 (24)	4.2 (187)	3.5 (108)	3.5 (60)

For the Fontainebleau samples, the MA and GR methods produce more isolated and 1-connected pores than the other methods, especially for the low porosity sample F11. This sample has significant amounts of quartz cementation which makes it difficult to identify the original grains. The GR method thus tends to identify grain clusters rather than individual grains. We also note that the maximum coordination number for the VB method is about twice that of the other methods. The reason for this is currently being investigated.

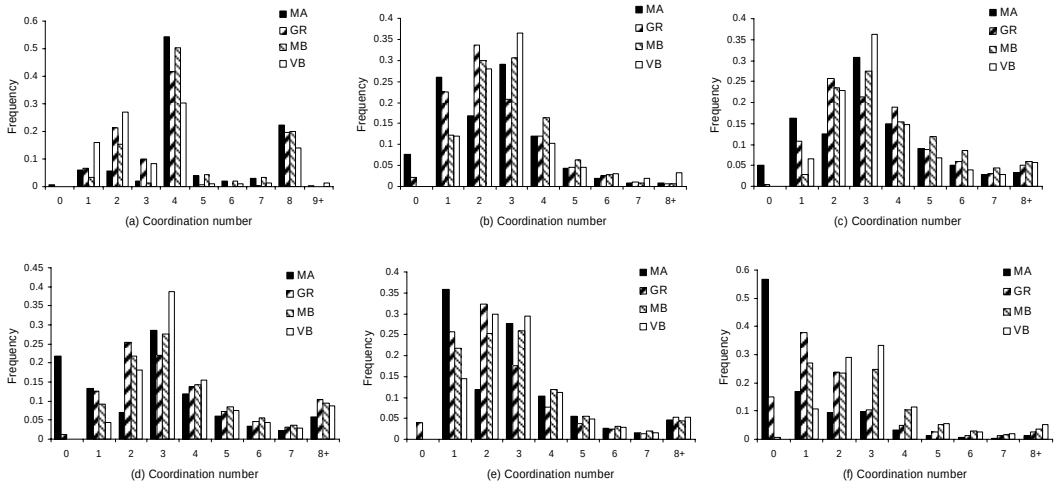

Figure 3. Coordination number distributions of samples. (a) P1; (b) F11; (c) F22; (d) C1; (e) C2 and (f) S1.

The level of noise in MCT images is generally higher than in PB images. The sensitivity of the different methods to image noise can thus be more clearly illustrated. Figure 3 shows that for the MCT images, the MA and GR methods find more 0- and 1- connected pores than the other methods. The 1-connected pores are small bumps on the solid surfaces while 0-connected pores are single points on the skeleton that can be artefacts of the method or actual isolated pores. For sample S1, more that 55% of the pores identified by the MA method is 0-connected. It seems physically unrealistic that the majority of pores in sandstone having intergranular porosity of 20% should be isolated; strongly suggesting that the large number of isolated pores is due to image noise. If we neglect the isolated pores, the average coordination number of the MA network increases from 1.1 to 2.6. Similarly, the coordination number for the GR network increases from 2.0 to 2.4.

Pore size distribution

Figure 4 shows the pore size distributions of all the networks. For sample P1, all the methods show a bi-modal pore size distribution. The locations of the main peak for the two distributions are also similar in the different networks. Differences are mainly found for small pore sizes that are associated with the image boundaries.

For the other samples, all the methods find a uni-modal pore size distribution with a long tail towards larger pore sizes. The pore size distribution of the high porosity sample C2 is almost identical for the different networks. For samples F11 and F22, the MB and GR networks are very similar. Compared to the MA and VB networks, the peaks in the MB and GR pore size distributions are located slightly towards larger pore sizes. This is also observed for sample C1. The MA pore size distribution for sample S1 differs clearly from the distributions found by the other methods. The height of the peak is larger and the location of the peak is at a smaller pore size. This is due to the large amount of small isolated pores present in the MA network.

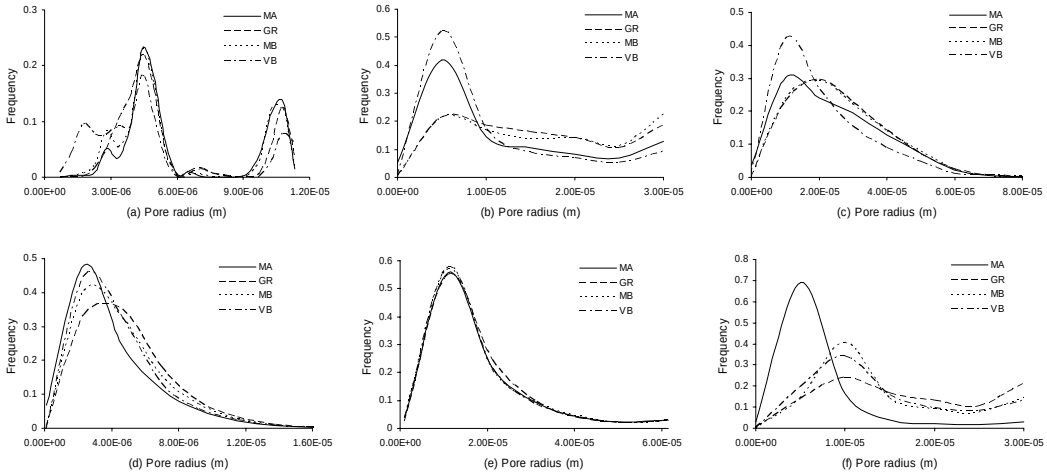

Figure 4. Pore body size distributions of samples; (a) P1; (b) F11; (c) F22; (d) C1; (e) C2 and (f) S1.

Throat size distribution

Figure 5 shows the pore throat size distributions of all the networks. Except for samples F11 and S1, the computed throat size distributions of a given sample are similar for all the networks. For sample F11, the peak in the distribution is much more distinct for the MA and VB networks than for the MB and GR networks. The average throat size of the GR network for sample F11 is also larger than that found by the other methods.

For sample S1, the GR throat size distribution is clearly different from the others. The distribution has no clear peak and it also has a higher frequency of larger throats. We also note that for sample C1, the GR throat size distribution is more flat in the vicinity of the peak found by the other methods. However, the average throat size for sample C1 is similar for all the networks.

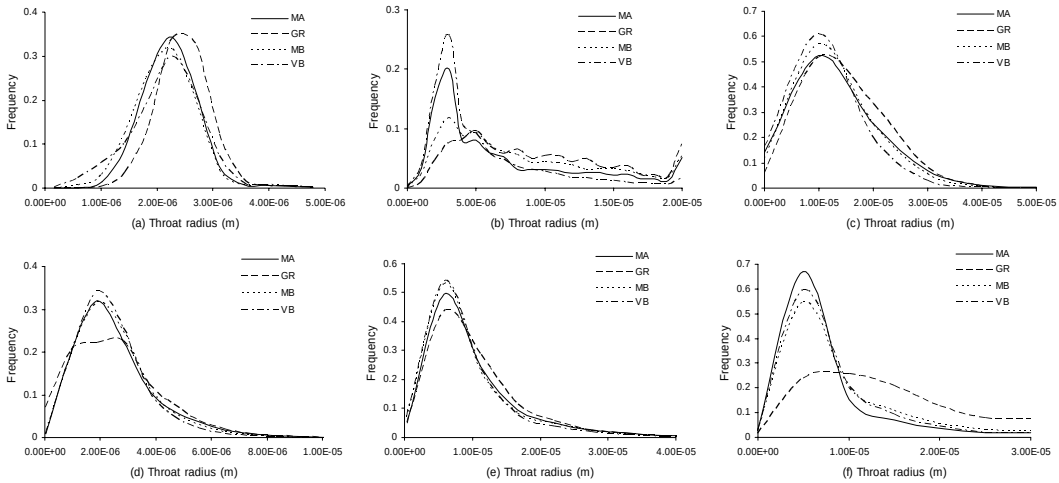

Figure 5. Throats size distributions of samples; (a) P1; (b) F11; (c) F22; (d) C1; (e) C2 and (f) S1.

TRANSPORT PREDICTIONS

We have implemented the extracted networks in a network model (Øren et.al., 1998) and computed single and multiphase properties. Network permeability and formation factor are compared to the directionally averaged results computed on the 3D images by solving the Stokes equations (Øren et.al., 2006) and the Laplace equation (Øren and Bakke, 2002) for the permeability and formation factor, respectively. Two-phase relative permeability for primary drainage and waterflooding under water wet conditions were calculated and compared for the networks extracted from the MCT images.

Single phase properties

Tables 3 and 4 summarize the predicted petrophysical properties of the networks. In most cases, the calculated permeability of the networks is larger than that computed on the voxel image. On average, the MB and VB networks over-predict the permeability with a factor 1.1. The corresponding values for the MA and GR are 1.3 and 1.7. For the GR networks, the largest permeability discrepancy is found for sample C2. This is probably due to the fact that the sample is not grain based. Excluding the regular packing sample P1, the permeability of the MB and VB networks are over-estimated by a factor of 0.99 and 1.03 on average. This indicates that the topological and geometrical properties, relevant for permeability predictions, are representative for the actual pore structures.

The computed formation factor of the networks is consistently lower than that calculated on the grid representation. On average, the networks under-predict the formation factor by approximately a factor 1.6. This suggests that the tortuousity of the network representations is smaller than that of the actual pore structures and/or that the electrical conductance (proportional to the cross-sectional area) is over-estimated.

The predicted permeability is mainly determined by the larger pore elements in the network, while the formation factors are influenced by the smaller ones. Excluding sample P1, the average over-estimation factor for permeability is 1.2, compared to an average under-estimation factor of 1.5 for formation factor. This indicates that the networks are representative for the interconnected large pores on the backbone skeleton while more careful investigations are required to optimize the descriptions of small crevices in the pore network. Nevertheless, the deviation on small pores can be theoretically improved by a finer image resolution.

Table 3. Absolute permeability of the voxel based image and networks.

	Voxel image	MA	GR	MB	VB
P1 (mD)	49	100	99	78	70
F11 (mD)	239	268	369	225	237
F22 (mD)	4167	4289	7610	4289	3912
C1 (mD)	336	370	634	351	367
C2 (mD)	24045	31863	46275	21139	23428
S1 (mD)	2403	3061	2428	2473	2807
Over-estimation factor		1.32	1.70	1.09	1.10

Table 4. Formation factors of the voxel based image and networks.

	Voxel image	MA	GR	MB	VB
P1	26.7	13.1	13.2	15.0	14.1
F11	83.4	53	50.0	53.3	50.7
F22	14.4	11.2	7.9	10.4	9.6
C1	9.3	6.2	4.8	5.6	5.9
C2	7.9	4.9	3.7	4.5	5.2
S1	17.7	18.1	30.1	16.5	19.4
Under-estimation factor		1.50	1.70	1.51	1.54

Primary drainage

The details of two-phase displacement mechanisms in primary drainage and waterflooding are given elsewhere (Øren et.al., 1998). Figure 7 depicts calculated primary drainage relative permeability curves on the different networks from the three MCT images. Considering the small size of the networks and the large percolation threshold effects, the differences in the computed relative permeabilities are small. Since the injected oil phase proceeds by invading the largest available pore element, this suggests that for a given sample the distribution and connectivity of the larger pore elements are similar between the different networks. The irreducible water saturation S_{wi} is determined by the water fraction associated with micro-porosity in clay, and isolated pore volumes. For sample S1, the S_{wi} is 0.27 for the MA network, compared to 0.24, 0.20 and 0.20 for the GR, MB and VB networks, respectively. The higher S_{wi} for the MA and GR networks are due to larger numbers of isolated pores.

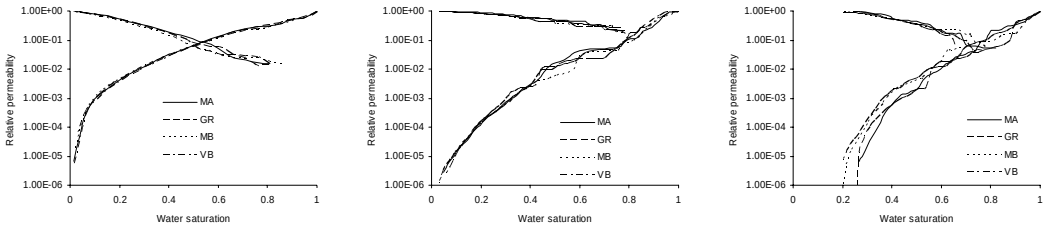

Figure 7. The primary drainage relative permeability of samples C1 (left), C2 (middle) and S1 (right).

Waterflooding

Figure 8 depicts the calculated waterflood relative permeability curves. In water wet systems, waterflooding proceeds by water preferentially invading the smallest (i.e. largest capillary entry pressure) available pore elements. The behaviour of the waterflood is thus sensitive to the distribution and connectivity of the smallest pore elements in the network. For samples C1 and C2, all the networks predict similar relative permeability curves. For sample C1, the residual oil saturations S_{or} for all the networks range from 0.27 to 0.32. For sample C2, the residual oil saturations are from 0.49 to 0.51 for MA, MB and VB networks, while it is 0.41 from the GR network. This relatively large variation can be caused by finite size effects (very small networks) or that the backbone skeleton of the GR network is better connected (although the GR network has the lowest average coordination number).

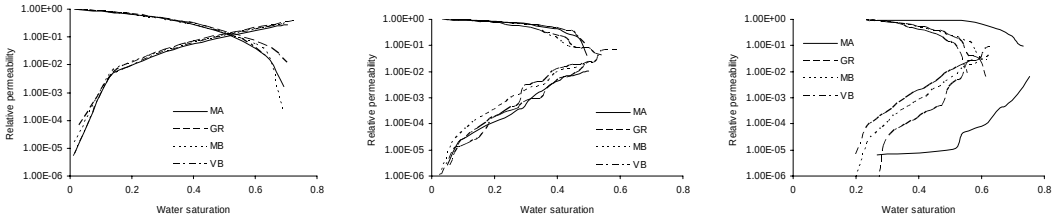

Figure 8. The waterflooding relative permeability of samples C1 (left), C2 (middle) and S1 (right).

For sample S1, the MA network behaves drastically different from the other networks. The water and oil relative permeabilities are almost constant over a large saturation range. This shows that many of the smaller pore elements are in the form of branches that do not form closed loops. Invasion of these branches contribute to saturation, but has little effect on the hydraulic conductance and thus the relative permeability. The shape of the computed relative permeability curve is rather unphysical for water wet systems, suggesting that the MA network is a poor representation of the actual pore structure. The main reason for this is probably the presence of clay and image noise. As for sample C2, we observe that although the GR network has the lowest average coordination number, the computed residual oil saturation (0.38) is similar to that of the MB network (0.38) and VB network (0.41).

CONCLUSION

Four methods (MA, GR, MB and VB) have been applied to extract topological skeletons from 3D images of sandstones and carbonates. The complete pore networks are extracted from the computed skeletons using the same algorithm for geometrical partitioning and analysis. The structural and predicted transport properties of the networks are compared.

For all the samples analysed, the MA and GR methods produce networks which contain more isolated and 1-connected pores than the MB and VB networks. For the sample with highest level of noise (sample S1), the applied MA algorithm failed to identify a realistic pore network. Pore sizes determined by the VB and MB networks tend to be similar. The pore sizes for the MA and GR networks are also similar (except for sample S1), but slightly larger than those of the VB and MB networks.

The networks tend to over-predict the permeability compared to the one computed directly on the voxel image. On average, the MB and VB networks over-predict the permeability by a factor of 1.1. The corresponding value for the MA and GB networks are 1.3 and 1.7, respectively. All the networks under-predict the formation factor roughly by a factor 1.6. This suggests that the tortuousity of the network representations is smaller than that of the actual pore structures.

The predicted primary drainage relative permeability curves for the three MCT samples are similar for all the networks. The computed imbibition relative permeabilities on the different networks are also similar for samples C1 and C2. For sample S1, the MA network predicts relative permeabilities that differ drastically from those computed on the other networks. The residual oil saturation for the GR networks tend to be smaller than that of the other networks. In general, we find that the MB and VB networks give similar transport predictions.

ACKNOWLEDGEMENTS

The authors acknowledge Numerical Rocks AS for granting permission to publish this paper. StatoilHydro ASA is also thanked for permission to publish the C1 and S1 data.

REFERENCES

Arns, C.K., Knackstedt, M.A., Pinczewski, V.W., and Martys, N.S., “Virtual permeametry on micro-tomographic images”, J. Pet. Sci. Eng., (2004), **45**, 41-46.

Al-Kharusi, A.S. and Blunt, M.J., “Network extraction from sandstone and carbonate pore space images”, J. Pet. Sci. Eng., (2007), **56,** 219-231.

Baldwin, C.A., Sederman, A.J., Mantle, M.D., Alexander, P. and Gladden, L.F., “Determination and characterization of the structure of a pore space from 3D volume images”, Journal of Colloid and Interface Science, (1996) **181,** 79-92.

Bakke, S. and Øren, P.E., “3-D pore-scale modelling of sandstones and flow simulations in the pore networks”, SPEJ, (1997), **2**, 136-149.

Blunt, M.J., Jackson, M.D., Piri, M. and Valvatne, P.H., "Detailed physics, predictive capabilities and macroscopic consequences for pore-network models of multiphase flow", Advances in Water Resources, (2002) **25**, 1069-1089.
Bryant, S.L., Mellor, D.W., and Cade, C.A., "Physically representative network models of transport in porous media", AIChE J., (1993), **39**, 387-398.
Dong, H., "Micro CT imaging and pore network extraction", PhD thesis, (2007),
Department of Earth Science and Engineering, Imperial College
Liang, Z., Ioannidis, M.A. and Chatzis, I., "Geometric and topological analysis of three-dimensional porous media: pore space partitioning based on morphological skeletonization", Journal of Colloid and Interface Science, (2000) **221,** 13-24.
Lindquist, W.B., Lee, S.M., Coker, D., Jones, K. and Spanne, P., "Medial axis analysis of void structure in three-dimensional tomographic images of porous media", Journal of Geophysical Research, (1996) **101B,** 8297.
Patzek, T.W., "Verification of a complete pore network simulator of drainage and imbibition", SPE Journal, (2001) **6,** 144-156.
Sheppard, A.P., Sok, R.M. and Averdunk, H., " Improved pore network extraction methods", Proceedings of International Symposium of the Society of Core Analysts, Toronto, Canada (2005).
Silin, D. and Patzek, T., "Pore space morphology analysis using maximal inscribed spheres", Physica A, (2006) **371**, 336-360.
Spanne, P., Thovert, J.F., Jacquin, C.J., Lindquist, W.B., Jones, K.W., and Adler, P.M., "Synchrotron computed microtomography of porous media: topology and transport", Phys. Rev. Let., (1994), **73**, 2001-2004.
Thompson, K.E., Willson, C.S., White, C.D., Nyman, S., Bhattacharya, J. and Reed, A.H., "Application of a new grain-based reconstruction algorithm to microtomography images for quantitative characterization and flow modeling", SPE 95887, presented at SPE Annual Technical Conference and Exhibition held in Dallas, Texas (2005).
Øren, P.E., Bakke, S., and Arntzen, O.J., "Extending predicitive capabilites to network models", SPEJ, (1998), **3**, 324-336.
Øren, P.E. and Bakke, S., "Process Based Reconstruction of Sandstones and Prediction of Transport Properties", Transport in Porous Media, (2002) **46**, 311-343.
Øren, P.E. and Bakke, S., " Reconstruction of Berea Sandstone and Pore-Scale Modeling of Wettability Effects", Journal of Petroleum Science and Engineering, (2003) **39,** 177-199.
Øren, P.E., Bakke, S., and Rueslåtten, H.G., "Digital core laboratory: Rock and flow properties derived from computer generated rocks", Proceedings of International Symposium of the Society of Core Analysts, Trondheim, Norway (2006).
Youssef, S., Rosenberg, E., Gland, N., Bekri, S. and Vizika, O., "Quantitative 3D characterisation of the pore space of real rocks: improved μ-CT resolution and pore extraction methodology", Proceedings of International Symposium of the Society of Core Analysts, Calgary, Canada (2007).